Molecular Catalysis 535 (2023) 112864

Contents lists available at ScienceDirect

Molecular Catalysis

journal homepage: www.journals.elsevier.com/molecular-catalysis

Methane direct conversion to olefins, aromatics, and hydrogen over silica entrapped bimetallic MeFe-SiO_2 (Me = Co, Ni, Pd, Pt) catalysts

Seung Ju Han [a,1,*], Tsegay Gebrekidan Gebreyohannes [a,b,1], Sung Woo lee [a], Seok Ki Kim [c,d], Hyun Woo Kim [e], Jungho Shin [f], Yong Tae Kim [a,b,*]

[a] *C1 Gas and Carbon Convergent Research Center, Korea Research Institute of Chemical Technology (KRICT), 141 Gajeong-ro, Yuseong-gu, Daejeon 34114, Republic of Korea*
[b] *Department of Advanced Materials and Chemical Engineering, University of Science and Technology (UST), 217 Gajeong-ro, Yuseong-gu, Daejeon 34113, Republic of Korea*
[c] *Department of Chemical Engineering, Ajou University, Suwon 16499, Republic of Korea*
[d] *Department of Energy Systems Research, Ajou University, Suwon 16499, Republic of Korea*
[e] *Department of Chemistry, Gwangju Institute of Science and Technology (GIST), Gwangju 61005, Republic of Korea*
[f] *Chemical Data-Driven Research Center, Korea Research Institute of Chemical Technology (KRICT), 141 Gajeong-ro, Yuseong-gu, Daejeon 34114, Republic of Korea*

ARTICLE INFO

Keywords:
Non-oxidative methane conversion
Iron/silica catalyst
Natural gas
Bimetallic catalyst
Coke deposition

ABSTRACT

Here, MeFe-SiO_2 (Me = Co, Ni, Pd, Pt) catalysts with bimetallic sites entrapped in a highly crystalline SiO_2 structure were synthesized and used for the conversion of methane to olefins, aromatics, and hydrogen (MTOAH) at 1020°C. The MeFe-SiO_2 catalysts showed polymorphic forms of cristobalite, quartz, and tridymite after reaction. Among the bimetallic catalysts, 0.5Pt1.0Fe-SiO_2 exhibited the highest methane conversion (10.0%) with high hydrocarbon selectivity (79.9%) at 1020°C. In C_2 (ethane, ethylene, acetylene) conversion with hydrogen co-feeding at 1020°C, acetylene was identified as a major coke precursor. MTOAH with different gas hourly space velocities (GHSV) showed that the 0.5Pt1.0Fe-SiO_2 catalyst exhibited higher methane conversion and aromatics selectivity than the 1.0Fe-SiO_2 catalyst. Density functional theory calculations showed that the Pt-Fe_3C surface is energetically favorable for methane activation and inhibits graphitic coke deposition by C_2 dehydrogenation. Consequently, a modification of the entrapped Fe sites by Pt addition improved the methane conversion and hydrocarbon selectivity of the catalyst.

1. Introduction

To alleviate the global climate crisis caused by anthropogenic carbon emissions, the chemical industry, a major contributor to global carbon emissions, should be decarbonized [1]. With large reserves of shale gas, natural gas, and methane hydrate, on-site methane-to-chemical conversion is expected to replace fossil fuels in the future [2,3]. The non-oxidative conversion of methane (NOCM) to chemicals has attracted immense attention owing to its high carbon efficiency and lack of CO_2 generation. Methane dehydroaromatization (MDA) to benzene, toluene, and xylene (BTX) has been extensively studied since the first publications reporting Mo/HZSM-5 [4,5]. However, methane activation requires high reaction temperatures (> 700°C), at which coke formation is thermodynamically favored [6]. To overcome this limitation, methane pyrolysis has been carried out at high temperatures (> 1000°C). However, severe coking is unavoidable at high reaction temperatures, and the studies have mainly focused on the process parameters of methane pyrolysis; the C_2 product selectivity has been enhanced by maintaining short residence times and diluting methane with hydrogen [7]. In 2014, Bao et al. have reported the efficient conversion of methane to olefins, aromatics, and hydrogen (MTOAH) using an Fe single-atom catalyst under non-oxidative conditions (> 1000°C) [8]. The role of the Fe single-atom catalyst that selectively catalyzes methane has been investigated further by computational studies [9]. After the development of an Fe©SiO_2 catalyst, numerous studies have focused on the experimental and theoretical analyses of silica-confined single-atom catalysts for the NOCM. Xie et al. have developed a $Pt_1@CeO_2$ single-atom catalyst with higher catalytic activity than Fe©SiO_2 [10], Liu et al.

---

* Corresponding authors.
E-mail addresses: hansj@krict.re.kr (S.J. Han), ytkim@krict.re.kr (Y.T. Kim).

[1] These authors contributed equally to this work.

https://doi.org/10.1016/j.mcat.2022.112864
Received 18 September 2022; Received in revised form 4 December 2022; Accepted 5 December 2022

have theoretically proposed a surface-reaction mechanism explaining the withdrawal of carbon sites on Fe©SiO_2 to form C_2 species [11], Han et al. have proposed an efficient NOCM process using an Fe©CRS catalyst with hydrogen co-feeding [12], and Dixit et al. theoretically studied methane activation on iron carbide clusters embedded in silica [13]. Furthermore, Postma et al. have reported that the axial temperature profile and residence time significantly influence radical-chain-reaction propagation in the downstream direction [14]. According to Toraman et al., the gas-phase reaction should be minimized for high ethylene selectivity in the NOCM using an Fe©SiO_2 catalyst [15]. Thus, catalyst selection and process-parameter optimization can effectively control the product selectivity in the NOCM. Process-optimization studies involving the millisecond wall reactor [16] and H-donor molecule addition [17, 18] have been used to analyze the practicability of the NOCM. Huang et al. have reported an economically-feasible direct non-oxidative methane conversion with a one-pass methane conversion of more than 25% and coke selectivity of less than 20% [19].

Numerous studies on promoters have focused on improving the catalytic activity and selectivity of direct methane conversion [20–24]. In MDA over Mo/zeolite catalysts, Fe and K effectively reduce coke deposition [25]. At 800°C, an Mg-modified Mo/HZSM-5 catalyst exhibits higher methane conversion (12.3%) than an unmodified Mo/HZSM-5 catalyst [26]. Additionally, Xiao et al. have proposed a Pt-Bi catalyst for methane non-oxidative coupling with high methane conversion and carbon selectivity [27]. Furthermore, bimetallic catalysts have been used for efficient methane non-oxidative conversion at high temperatures ($>$ 900°C). Ni et al. have reported that molten W-In bimetals confined in SiO_2 exhibit high catalytic activity and coke resistance [28].

According to an ideal mechanism, Fe sites selectively activate methane, causing a chain reaction of methyl radicals [12]; the C-H bond of C_2 intermediates and aromatics are readily activated on the catalyst, causing coke deposition [9]. Therefore, controlling the reactivity of the C_2 intermediate at the Fe site can improve the selectivity of the desired products. In this study, MeFe-SiO_2 catalysts (Me = Co, Ni, Pd, Pt) with high crystallinity were synthesized using the melt-fusing method to investigate the effect of bimetallic Me-Fe sites on catalytic activity. The physicochemical properties of the bimetallic catalysts were investigated by various techniques. A computational analysis was used to theoretically investigate the activity of the bimetallic active phase. This study elucidates the role of bimetallic catalysts and their potential applicability in non-oxidative methane conversion processes.

2. Materials and Methods

2.1. Chemicals

Fe (II) chloride ($FeCl_2$, 99.5%) was purchased from Alfa Aesar. Sodium ethoxide ($NaOC_2H_5$, 95%), tetraethyl orthosilicate ($Si(OC_2H_5)_4$, 98% reagent grade), and Pd (II) nitrate dihydrate ($Pd(NO_3)_2{\cdot}2H_2O$, 40% Pd basis) were purchased from Sigma-Aldrich. NaOH (98%), anhydrous methanol (CH_3OH, 99.5%), toluene ($C_6H_5CH_3$, 99.5%), cobalt (II) nitrate hexahydrate ($Co(NO_3)_2{\cdot}6H_2O$, 97%), and nickel (II) nitrate hexahydrate ($Ni(NO_3)_2{\cdot}6H_2O$, 98%) were purchased from Samchun Chemicals. Tetraammineplatinum (II) nitrate ($Pt(NH_3)_4(NO_3)_2$, 99%) was purchased from Strem Chemical. Silicon dioxide (SiO_2, quartz form) was purchased from Kanto. All the chemicals were used without further purification.

2.2. Synthesis of Fayalite

Fe_2SiO_4 (fayalite) was synthesized by a previously reported sol-gel method [29,30]. A toluene (375 mL) and methanol (175 mL) mixture was purged at 250°C for 30 min under Ar. Subsequently, the mixture was cooled to room temperature, followed by the addition of iron (II) chloride (8.7 g) and sodium ethoxide (9.3 g). After rigorous stirring for a minute, 7.9 g of tetraethyl orthosilicate (TEOS) was added to the solution, after which it was refluxed at 150°C for 30 min under Ar. Subsequently, 10 mL of 0.2 M sodium hydroxide solution was added to induce the sol-gel process by hydrolyzing iron oxide and TEOS. The solution was then refluxed at 150°C for 12 h under Ar. The resulting solution was finally dried by rotary evaporation and the dry powder obtained was calcined at 800°C for 4 h under nitrogen. After calcination, the solid was rinsed with distilled water (D.I. water) and methanol to remove any unreacted sodium chloride. Finally, the samples were dried overnight in an oven at 80°C.

2.3. Synthesis of Me/SiO_2 (Me = Co, Ni, Pd, Pt)

Me/SiO_2 (Me = Co, Ni, Pd, Pt) was synthesized using the incipient-wetness-impregnation method. Cobalt (II) nitrate hexahydrate, nickel (II) nitrate hexahydrate, palladium (II) nitrate dehydrate, and tetraamine platinum (II) nitrate were used as metal precursors for Me/SiO_2 synthesis. After the dissolution of a specific amount of metal precursor in 50 mL of D.I. water, silicon dioxide was added to the solution and stirred vigorously. Subsequently, the solution was dried overnight at 120°C and the dry powder obtained was calcined at 400°C for 4 h at a heating rate of 2°C/min.

2.4. Synthesis of Fe-SiO_2 and MeFe-SiO_2 (Me = Co, Ni, Pd, Pt) catalysts

The Fe-SiO_2 catalyst was synthesized by a previously reported melt-fusing method [8,12]. Silicon dioxide (6 g) and fayalite (0.112 g) were mixed by the ball-milling technique at 250 rpm for 5 h under Ar. Subsequently, this mixed powder was melt-fused at 1700°C for 4 h at a ramping rate of 8°C/min. To synthesize the MeFe-SiO_2 (Me = Co, Ni, Pd, Pt) catalysts, Me/SiO_2 (6 g) and fayalite (0.112 g) were mixed and melt-fused at 1700°C for 4 h at a ramping rate of 8°C/min. The synthesized catalysts were labeled xMeyFe-SiO_2 (x and y represent the content (wt%) of Me and Fe, respectively).

2.5. Characterization

Inductively coupled plasma-atomic emission spectroscopy (ICP-AES, Thermo Scientific, iCAP 6500 instrument) was used to analyze the metal compositions of the synthesized catalysts, while X-ray diffraction (XRD, Rigaku SmartLab diffractometer, using Cu-Kα radiation) was used to investigate their crystalline structures. The specific surface areas of the catalysts were estimated by N_2 adsorption-desorption measurements (Micromeritics ASAP2010). A gas pycnometer (AccuPyc II 1340, Micromeritics) was used to measure the catalyst density; density calculations were based on a gas-displacement method using He as the displacement medium [31]. Free space was obtained by subtracting catalyst volume from the reaction volume (1.09 ml). The catalyst morphologies were observed by transmission electron microscopy (TEM) using an FEG S/TEM instrument (Talos F200S) operated at 200 kV. The amount of coke deposited on the used catalysts was measured by thermogravimetric analysis (TGA) using an SDT Q600 instrument (TA instruments); each sample (30–40 mg) was heated from room temperature to 900°C at a ramping rate of 5°C/min under a constant air flow (100 mL/min). The properties of coke deposited on the spent catalysts were analyzed by Raman spectroscopy using a Bruker FRA 106/S spectrometer.

2.6. Reaction test

A 1/4" quartz fixed-bed reactor with an inner diameter of 0.4 cm was used to analyze the CH_4 non-oxidative conversion. The temperature was controlled using R-type thermocouples (in contact with the outer part of the reactor). The catalyst (0.6 g) was loaded at a pre-designed position on the vertical reactor and heated under a pure-He-gas flow (at a rate of 40 sccm) at a ramping rate of 6 °C/min to a reaction temperature of 1020

°C. Subsequently, 10 sccm of a mixed gas (90% CH_4 and 10% Ar) was fed into the reactor.

The non-oxidative conversion of C_2 hydrocarbons (C_2H_6, C_2H_4, and C_2H_2) was conducted under the same pretreatment conditions, followed by a stabilization of the catalyst under 10 sccm of the mixed gas (90% CH_4 and 10% Ar) for 5 h. Subsequently, the mixed gas containing C_2 hydrocarbons was fed into the reactor according to the reaction scheme shown in Fig. S1. Each reactant gas was fed in a stream at a rate of 10 sccm for 5 h. The compositions of reactant gases used for ethane, ethylene, and acetylene conversion were 5% C_2H_6 and 5% H_2 in He, 5% C_2H_4 and 5% H_2 in He, and 1% C_2H_2 and 1% H_2 in He, respectively.

An online gas chromatograph (6100GC, YL Instrument) was used to analyze the gas composition of the reactor effluent stream, and a thermal conductivity detector (TCD) with a ShinCarbon ST column (Catalog No. 80486-800) was used to evaluate the amounts of H_2, CH_4, Ar, CO, CO_2, and C_2 (ethane, ethylene, and acetylene). The injection port and detector were maintained at 200°C, and the column flow rate of the He carrier gas was 20 mL/min. A flame ionization detector (FID) with an Rtx-VMS column (Restek, Catalog No. 49915) was used to analyze the C_1–C_5 hydrocarbons and aromatic compounds in methane conversion using He as a carrier gas with a column flow rate of 0.5 $ml\cdot min^{-1}$. Whereas, in the C_2-conversion reaction, a flame ionization detector (FID) with an RT-Alumina BOND column (Restek Corp., Catalog No. 19756) was used to analyze the C_1–C_5 hydrocarbons and aromatic compounds using He carrier gas (3.0 $ml\cdot min^{-1}$). In both cases, the injection port and detector temperatures were maintained at 200 and 250°C, respectively. The flow lines were maintained at the same temperature (140 °C) to prevent product condensation and the reaction utilized a gas hourly space velocity (GHSV) of 1,000 $ml\cdot h^{-1}g_{cat}^{-1}$.

2.7. Computational details

A plane-wave based Vienna ab initio simulation package (VASP) was used for the density functional theory (DFT) calculations [32,33]. The vdw-DF2 exchange-correlation functional was used under the generalized gradient approximation (GGA) [34–38] with a proper description of van der Waals interactions, while a 0.01 eV/Å convergence criterion was used for geometric approximation. For the bulk structure calculation of Fe_3C, an 8 × 8 × 8 Monkhorst–Pack k-point mesh grid was used. The (001) phase of Fe_3C was selected as the representative model, and a supercell with 12 formula units ($Fe_{36}C_{12}$) was optimized [39]. The supercells for Me-Fe_3C (001) (Me = Co, Ni, Pd, Pt) were constructed by substituting a surface Fe atom with an Me atom (Fig. S2). For optimization, a vacuum thickness of 15 Å was applied, keeping the units of the bottom layer fixed. A 4 × 4 × 1 Monkhorst–Pack k-point mesh grid was used for surface-slab calculations. The electronic formation energies for the gases and adsorbents were calculated considering the CH_4 and H_2 energies as references (Table S1) [40]. The Gibbs free formation energy of gases was calculated using the ideal-gas assumption, while those of the adsorbents were calculated using the harmonic limit [41].

3. Results and discussion

3.1. Characterization of MeFe-SiO_2 (Me = Co, Ni, Pd, Pt) Catalysts

Table 1 summarizes the physicochemical properties of the fused SiO_2, 1.0Fe-SiO_2, and 0.5Me1.0Fe-SiO_2 (Me = Co, Ni, Pd, Pt) catalysts. The catalysts exhibited Fe contents in the range of 0.7–0.8 wt%. Similar to the previous study, the fused SiO_2 and Fe catalysts synthesized by the melt-fusing method showed high crystallinity and low surface areas (< 3 m^2/g), even with the addition of a second metal [12]. Thus, the melt-fusing process at 1700°C formed a uniform liquid phase of fayalite, a second metal (Co, Ni, Pd, Pt), and quartz, enabling the 0.5Fe-SiO_2 and 0.5Me0.5Fe-SiO_2 catalysts to exhibit high crystallinity and low surface area (< 3 m^2/g) (Table S2). The catalyst density, estimated by a gas pycnometer, was in the range of 2.2–2.4 g/cm^3 (Table 1). It was observed that 0.5Me1.0Fe-SiO_2 catalyst showed relatively higher BET surface area compared to fused SiO_2 and 1.0Fe-SiO_2 catalyst. This might be due to that addition of second metal induced segregation of Fe oxides and inhibits densification of silica structure during the melt-fusing step.

Fig. 1 represents the XRD patterns of the fresh and used 0.5Me1.0Fe-SiO_2 catalysts (Me = Co, Ni, Pd, Pt). All the catalyst XRD patterns exhibited high-intensity peaks corresponding to cristobalite (PDF NO. 1-438), indicating the transformation of the quartz form of silica into α-cristobalite during the melt-fusing process. No significant peaks were observed for Fe species, indicating the predominant formation of high-dispersion Fe oxide, possibly due to silica-matrix confinement. In the XRD patterns for 0.5Co1.0Fe-SiO_2 and 0.5Ni1.0Fe-SiO_2 catalyst, no significant peaks for oxide forms and metallic forms of Co and Ni were observed. This might be due to their small content and high dispersion on the silica structure. While, the 0.5Pd1.0Fe-SiO_2 and 0.5Pt1.0Fe-SiO_2 exhibited metallic forms of the secondary metals (Pd and Pt) with high crystallinity, indicating that the metallic species in 0.5Pd1.0Fe-SiO_2 and 0.5Pt1.0Fe-SiO_2 aggregated due to their reducibility differences with iron. The sizes of the primary catalyst crystals were estimated using the cristobalite diffraction peak at $2\theta = 22.0^\circ$ (Table 1 and Fig. 1). The 0.5Me1.0Fe-SiO_2 catalysts showed a relatively high surface area with smaller crystalline cristobalite sizes than those of fused SiO_2 and 1.0Fe-SiO_2. This could be attributed to a silica-structure relaxation during the melt-fusing process due to the high transition-metal content of the catalysts [42]. Fig. 1(b) shows the XRD patterns for the 0.5Me1.0Fe-SiO_2 catalysts after a 10-h methane-conversion reaction at 1020°C. Peaks corresponding to graphitic coke were observed in the patterns of the used catalysts, which could be attributed to coke deposition during the reaction. Additionally, the Fe-oxide species were reduced to metallic Fe and Fe_3C. Interestingly, the peak intensities of the second metal decreased after reaction over 0.5Pd1.0Fe-SiO_2 and 0.5Pt1.0Fe-SiO_2, indicating a redispersion of mobile Pd and Pt atoms on the Fe surface at high reaction temperatures. The cristobalite form was maintained in fused SiO_2 and 0.5Fe-SiO_2, whereas polymorphic forms of cristobalite, quartz, and tridymite appeared in 1.0Fe-SiO_2 and 0.5Me1.0Fe-SiO_2 (with higher transition-metal contents) (Fig. S3) [42].

Table 1

Physicochemical properties of fused SiO_2, 1.0Fe-SiO_2, and 0.5Me1.0Fe-SiO_2 (Me = Co, Ni, Pd, Pt) catalysts.

Catalyst	Metal content [a] (wt%)					S_{BET} [b] (m^2/g)	Primary crystalline size of CRS (nm) [c]	Density [d] (g/cm^3)
	Fe	Co	Ni	Pd	Pt			
Fused SiO_2	-	-	-	-	-	0.60	61.6	2.31
1.0Fe-SiO_2	0.75	-	-	-	-	0.33	60.2	2.23
0.5Co1.0Fe-SiO_2	0.75	0.37	-	-	-	1.22	21.2	2.24
0.5Ni1.0Fe-SiO_2	0.72	-	0.40	-	-	1.39	31.0	2.20
0.5Pd1.0Fe-SiO_2	0.77	-	-	1.05	-	1.24	36.7	2.25
0.5Pt1.0Fe-SiO_2	0.76	-	-	-	0.39	1.24	32.5	2.21

[a] Amount of Fe was determined by ICP-AES.

[b] The BET surface area was determined by N_2 adsorption data.

[c] Primary crystalline size was measured by Scherrer equation.

[d] The catalyst density was measured by a gas pycnometer.

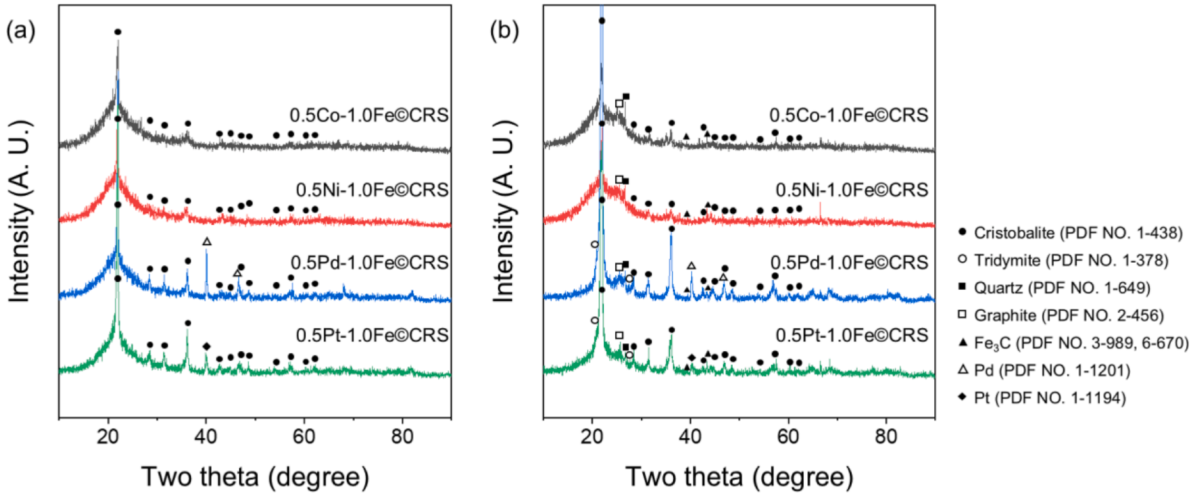

Fig. 1. X-ray diffraction patterns for (a) as-prepared and (b) used 0.5Me1.0Fe-SiO_2 (Me = Co, Ni, Pd, Pt) catalysts.

3.2. *Catalytic activity*

Methane-conversion reactions over the 0.5Me1.0Fe-SiO_2 catalysts at 1020°C were used to investigate the influence of the second-metal addition (Figs. 2 and 3). As shown in Fig. 2(a), fused SiO_2 showed the highest methane conversion among the as-prepared catalysts. At high temperatures, the silica surface exhibits good methane-conversion activity; thus, the high activity of fused SiO_2 could be attributed to its defect sites [12]. Unlike catalysis with blank and fused SiO_2, coke selectivity using 1.0Fe-SiO_2 increased during the first 5 h of catalysis, indicating a stabilization of the active metal by carburization or coke deposition. Fig. 3 shows the methane conversion and product selectivity over the 0.5Me1.0Fe-SiO_2 catalysts (Me = Co, Ni, Pd, Pt). Similar to 1.0Fe-SiO_2 catalysis, the C_2 selectivity decreased and coke selectivity increased during the first 5 h of catalysis. The 0.5Me1.0Fe-SiO_2 catalysts (Me = Co, Ni, Pt) exhibited higher methane conversions than the 1.0Fe-SiO_2 catalyst; 0.5Pt1.0Fe-SiO_2 exhibited low coke selectivity, with the high methane conversion after stabilization.

Table 2 summarizes the average methane conversion and product selectivity values over the catalysts during MTOAH reactions for 2–10 h. Among the reaction tests, the blank test showed the lowest methane conversion (3.9%) and the lowest normalized methane conversion rate (0.9 $mmol \cdot h^{-1} \cdot ml^{-1}_{free\ space}$). This shows that catalyst surface promotes C-H activation at the given reaction condition. The addition of Ni and Co increased coke selectivity and decreased C_2 selectivity compared to those of the 1.0Fe-SiO_2 catalyst, indicating that the co-existence of Ni

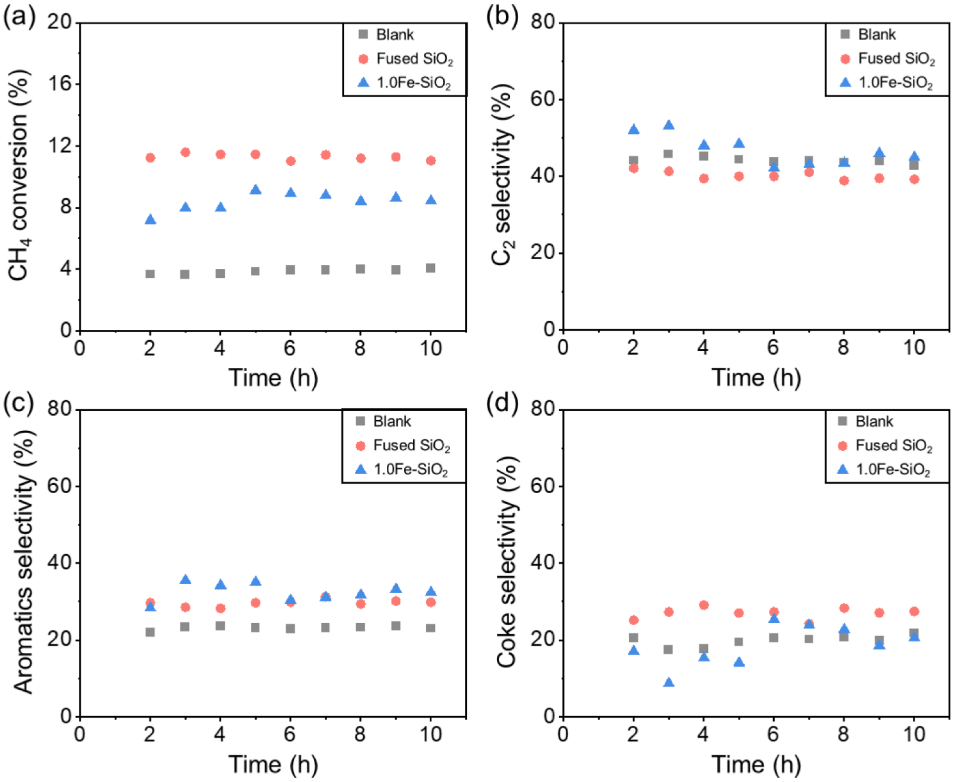

Fig. 2. CH_4 conversion and product selectivities over blank, fused SiO_2, and 1.0Fe-SiO_2 catalysts on stream. (a) Methane conversion, (b) C_2 selectivity, (c) aromatics selectivity, and (d) coke selectivity (Reaction condition: P_{total} = 1 bar, P_{CH4} = 0.9 bar, T = 1020°C, Catalyst = 0.6 g, GHSV = 1,000 $ml \cdot h^{-1} \cdot g_{cat}^{-1}$).

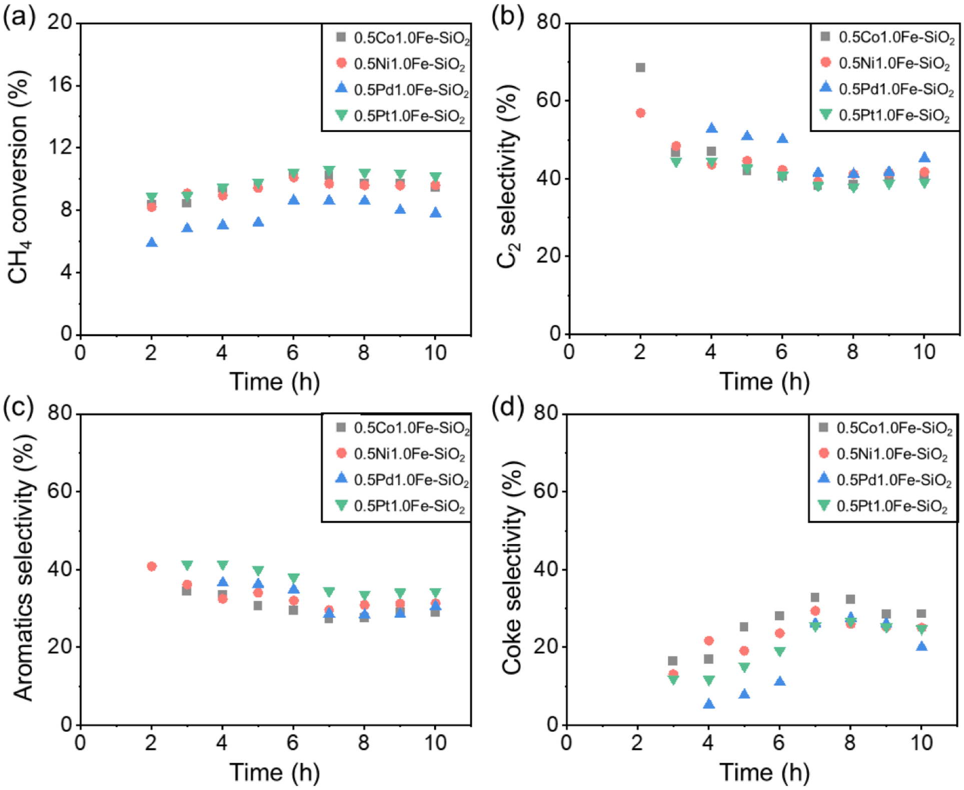

Fig. 3. CH_4 conversion and product selectivities over 0.5Me1.0Fe-SiO_2 catalysts (Me = Co, Ni, Pd, Pt) on stream (a) Methane conversion, (b) C_2 selectivity, (c) aromatics selectivity, and (d) coke selectivity (Reaction condition: $P_{total} = 1$ bar, $P_{CH4} = 0.9$ bar, T = 1020°C, Catalyst = 0.6 g, GHSV = 1,000 $ml \cdot h^{-1} \cdot g_{cat}^{-1}$).

Table 2

Average methane conversion and product selectivity over fused SiO_2, 1.0Fe-SiO_2, and 0.5Me1.0Fe-SiO_2 (Me = Co, Ni, Pd, Pt) catalysts during a 2-10 h MTOAH reaction (Reaction condition: $P_{total} = 1$ bar, $P_{CH4} = 0.9$ bar, T = 1020°C, Catalyst = 0.6 g, GHSV = 1,000 $ml \cdot h^{-1} g_{cat}^{-1}$).

Catalyst		Blank	Fused SiO_2	1.0Fe-SiO_2	0.5Co 1.0Fe-SiO_2	0.5Ni 1.0Fe-SiO_2	0.5Pd 1.0Fe-SiO_2	0.5Pt 1.0Fe-SiO_2
Methane conversion (%)		3.9 ± 0.1	11.3 ± 0.2	8.5 ± 0.4	9.6 ± 0.6	9.5 ± 0.4	8.0 ± 0.7	10.0 ± 0.6
Molar carbon selectivity (%)	*C_2*	44.2 ± 0.8	39.9 ± 0.9	46.1 ± 3.0	41.8 ± 3.4	42.8 ± 2.8	46.2 ± 5.0	40.8 ± 2.8
	C_3-C_5	12.9 ± 0.4	3.2 ± 0.3	2.3 ± 0.2	2.1 ± 0.2	2.1 ± 0.2	4.2 ± 0.8	2.0 ± 0.2
	Aromatics	23.1 ± 0.5	29.6 ± 0.9	33.0 ± 1.9	30.1 ± 2.7	32.2 ± 2.1	31.9 ± 3.8	37.1 ± 3.4
	Coke	19.8 ± 1.3	27.2 ± 1.4	18.6 ± 5.6	26.1 ± 6.3	22.9 ± 5.0	17.7 ± 9.5	20.0 ± 6.4
C_2 distribution (%)	*Ethane*	11.7	4.4	5.4	5.0	5.1	5.5	5.1
	Ethylene	62.6	62.6	63.1	63.3	63.0	63.3	61.9
	Acetylene	25.7	33.0	31.6	31.8	31.8	31.2	33.0
Aromatic distribution (%)	*Benzene*	59.8	62.9	60.8	61.5	61.5	60.4	61.5
	Toluene	16.2	10.3	11.9	11.4	11.3	12.9	10.6
	Naphthalene	9.9	13.6	12.3	13.1	13.4	12.2	15.0
	Alkyl aromatics	14.1	13.2	15.0	13.9	13.8	14.5	12.8
Carbon deposit (wt%)[a]		-	10.3	6.9	7.6	5.3	6.1	7.9
Normalized methane conversion rate ($mmol \cdot h^{-1} \cdot ml_{free\ space}^{-1}$)[b]		0.9	2.6	2.0	2.2	2.2	1.8	2.3

[a] Amounts of carbon on spent catalysts were determined by TGA under air (Fig. 7).

[b] Normalized methane conversion rate was measured by dividing the conversion rate by the free space.

and Co with Fe promoted C_2 conversion to aromatics and coke. Among the catalysts, 0.5Pt1.0Fe-SiO_2 exhibited a relatively high methane conversion (10.0%) with high aromatic selectivity (37.1%) and low coke selectivity (20.0%), indicating that the proximity of the Pt surface to the Fe site induced the termination of aromatics and inhibited coke formation. The 0.5Pd1.0Fe-SiO_2 catalyst exhibited methane conversion and coke selectivity values similar to those of 1.0Fe-SiO_2, possibly due to severe sintering and coke deposition in the Pd sites during the initial reaction time. Bimetallic catalysts exhibited higher normalized methane conversion rate than 1.0Fe-SiO_2 catalyst and among the Fe-containing catalysts 0.5Pt1.0Fe-SiO_2 catalyst showed the highest value (2.3 $mmol \cdot h^{-1} ml_{free\ space}^{-1}$).

The MTOAH reaction over 0.5Fe-SiO_2 and 0.5Me0.5Fe-SiO_2 (Me = Co, Ni, Pd, Pt) was conducted at 1020°C, as depicted in Fig. S5 and Table S3. Compared to fused SiO_2, the aromatics selectivity increased, while the coke selectivity decreased, on increasing the Fe content of the catalyst (aromatics selectivity values: fused SiO_2 (29.6%) ≈ 0.5Fe-SiO_2 (29.5%) < 1.0Fe-SiO_2 (33.0%), coke selectivity: 1.0Fe-SiO_2 (18.6%) < 0.5Fe-SiO_2 (24.2%) < fused SiO_2 (27.2%)). This could be attributed to a reduction in the number of cristobalite defect sites by the dense Fe crystals on the catalyst which hindered coke formation. Similar to 0.5Co1.0Fe-SiO_2, the 0.5Co0.5Fe-SiO_2 catalyst showed high methane

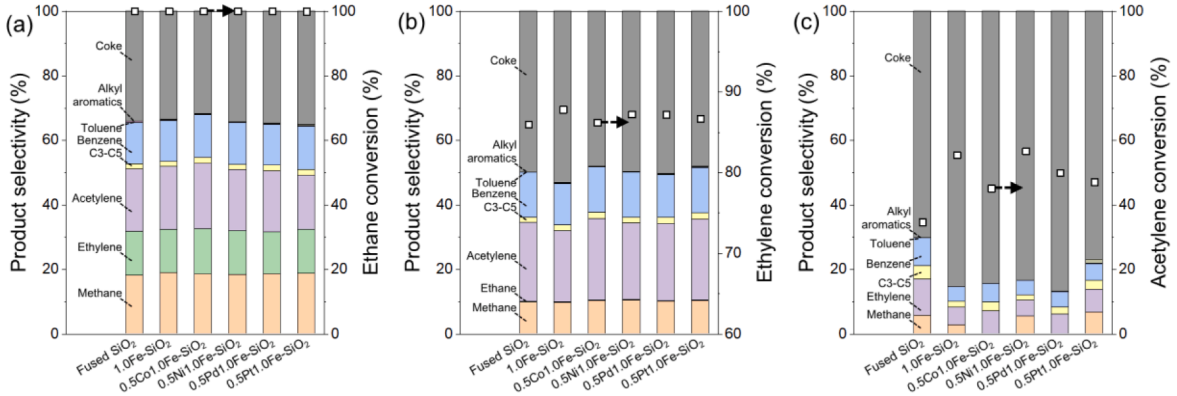

Fig. 4. C_2 ((a) ethane, (b) ethylene, and (c) acetylene) conversion and molar carbon selectivity over fused SiO_2, 1.0Fe-SiO_2, and 0.5Me1.0Fe-SiO_2 (Me = Co, Ni, Pd, Pt) catalysts (Reaction condition: (a) $P_{total} = 1$ bar, $P_{C2H6} = 0.05$ bar, $P_{H2} = 0.05$ bar, (b) $P_{total} = 1$ bar, $P_{C2H4} = 0.05$ bar, $P_{H2} = 0.05$ bar, (c) $P_{total} = 1$ bar, $P_{C2H2} = 0.01$ bar, $P_{H2} = 0.01$ bar. T = 1020°C, Catalyst = 0.6 g, GHSV = 1,000 $ml \cdot h^{-1} g_{cat}^{-1}$).

conversion (9.8%) and coke selectivity (30.1%). This could be attributed to high methane activation and C_2 dehydrogenation by the FeCo alloy sites, causing significant coke formation.

C_2 (ethane, ethylene, and acetylene) conversion with hydrogen co-feeding at 1020°C was conducted to identify the major coke precursor during MTOAH and compare the coke deposition over C_2 conversion (Fig. 4(a)–(c)). Considering the methane-conversion results (Figs. 2 and 3), the catalysts were stabilized with a methane feed for 5 h before the C_2-conversion reaction. The feed composition and flow rate profiles during C_2 conversion are shown in Fig. S1. In ethane hydrogenation, all the catalysts showed 100% conversion due to the thermodynamic instability of ethane at high temperatures [43]. In ethane and ethylene hydrogenation, the 0.5Pt1.0Fe-SiO_2 catalyst showed slightly higher aromatic selectivity (13.6% and 14.2%, respectively) than the 1.0Fe-SiO_2 catalyst (12.8% and 13.1%, respectively). Coke selectivity increased in the order of $C_2H_6 < C_2H_4 < C_2H_2$, even on using the most dilute feed (1% C_2H_2 + 1% H_2) for C_2H_2 hydrogenation. Notably, 0.5Pt1.0Fe-SiO_2 catalyst exhibited a lower acetylene conversion with lower coke selectivity compared to 1.0Fe-SiO_2 catalyst.

In order to investigate the effect of the bimetallic site under the shorter contact time for the reactant, the methane conversion reaction was conducted over 1.0Fe-SiO_2 and 0.5Pt1.0Fe-SiO_2 catalysts under various gas hourly space velocities (GHSV) (Fig. 5). Similar to the results under GHSV of 1,000 $ml \cdot h^{-1} g_{cat}^{-1}$ (Table 2), 0.5Pt1.0Fe-SiO_2 catalyst showed higher methane conversion and aromatics selectivity than 1.0Fe-SiO_2 catalyst. This demonstrates that the modification of Fe site by Pt addition promotes methane activation and aromatics termination, resulting in high hydrocarbon selectivity.

3.3. *Post-reaction analyses of spent catalysts*

The properties of the coke deposited on the used catalysts were analyzed by Raman spectroscopy (Fig. 6). The Raman spectra of the used catalysts were deconvoluted into five Lorentz peaks, according to previous publications [44,45]: the C-H vibration band at 1200 cm^{-1} ($I_{C\text{-}H}$), G-band for graphitic carbon at 1550–1600 cm^{-1} (I_G), and three types of D-bands for aromatic coke at 1350 cm^{-1} (I_{D1}), 1600–1610 cm^{-1} (I_{D2}), and 1450–1510 cm^{-1} (I_{D3}). The graphitic properties of the deposited coke were estimated using the area ratio of I_G to I_{D2} (Table 3). Among the catalysts, 1.0Fe-SiO_2 exhibited the highest I_G/I_{D2} ratio (3.78), indicating that graphitic coke deposited on the Fe surface was the major coke species in the 1.0Fe-SiO_2 catalyst. The I_G/I_{D2} ratio of the 0.5Me1.0Fe-SiO_2 catalyst (3.15-3.23) was lower than that of the 1.0Fe-SiO_2 catalyst, indicating that graphitic-coke deposition by the subsequent dehydrogenation of methane was inhibited on the bimetallic surface of the catalyst. Among the catalysts, 0.5Pt1.0Fe-SiO_2 showed the lowest I_G/I_{D2} ratio (3.15), consistent with its highest aromatic selectivity in MTOAH (Table 2).

TGA was used to analyze coke deposition (Fig. 7). The DTA profile of 1.0Fe-SiO_2 (Fig. 7(b)) exhibited a single band for coke oxidation at the lowest temperature (~690°C), indicating the predominant formation of graphitic coke (in close proximity to the Fe site) on the Fe-SiO_2 catalyst, in agreement with the Raman-spectra results (Fig. 6 and Table 3). The other catalysts exhibited coke-oxidation bands at positions similar to that exhibited by fused SiO_2 at high temperatures (> 720°C). This could be because the amount of aromatic-derived coke on the SiO_2 surface was higher on the bimetallic catalyst than on the 1.0Fe-SiO_2 catalyst.

TEM-EDS mappings of the 1.0Fe-SiO_2 and 0.5Me1.0Fe-SiO_2 catalysts after a 10-h methane conversion reaction were used to investigate the catalyst morphologies (Fig. 8). Fe particles with sizes in the range of

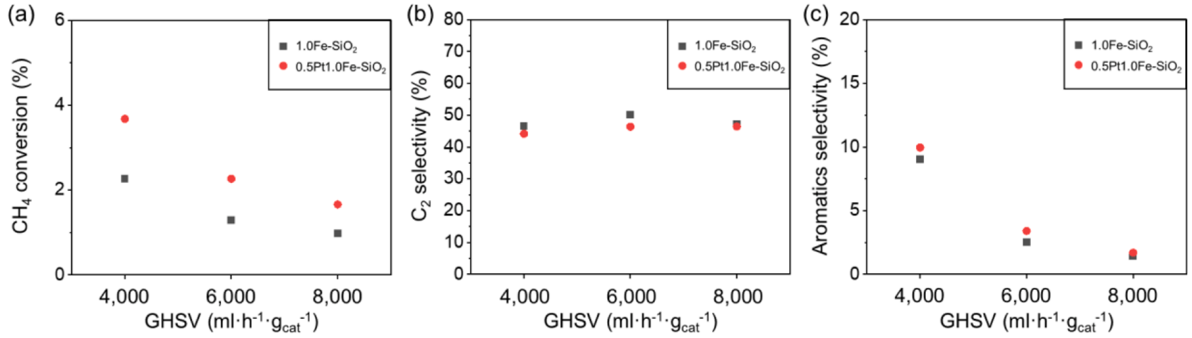

Fig. 5. (a) CH_4 conversion, (b) C_2 selectivity, and (c) aromatics selectivity over 1.0Fe-SiO_2, and 0.5Pt1.0Fe-SiO_2 catalysts, plotted as a function of GHSV (Reaction condition: $P_{total} = 1$ bar, $P_{CH4} = 0.9$ bar, T = 1020 °C, Catalyst = 0.3 g).

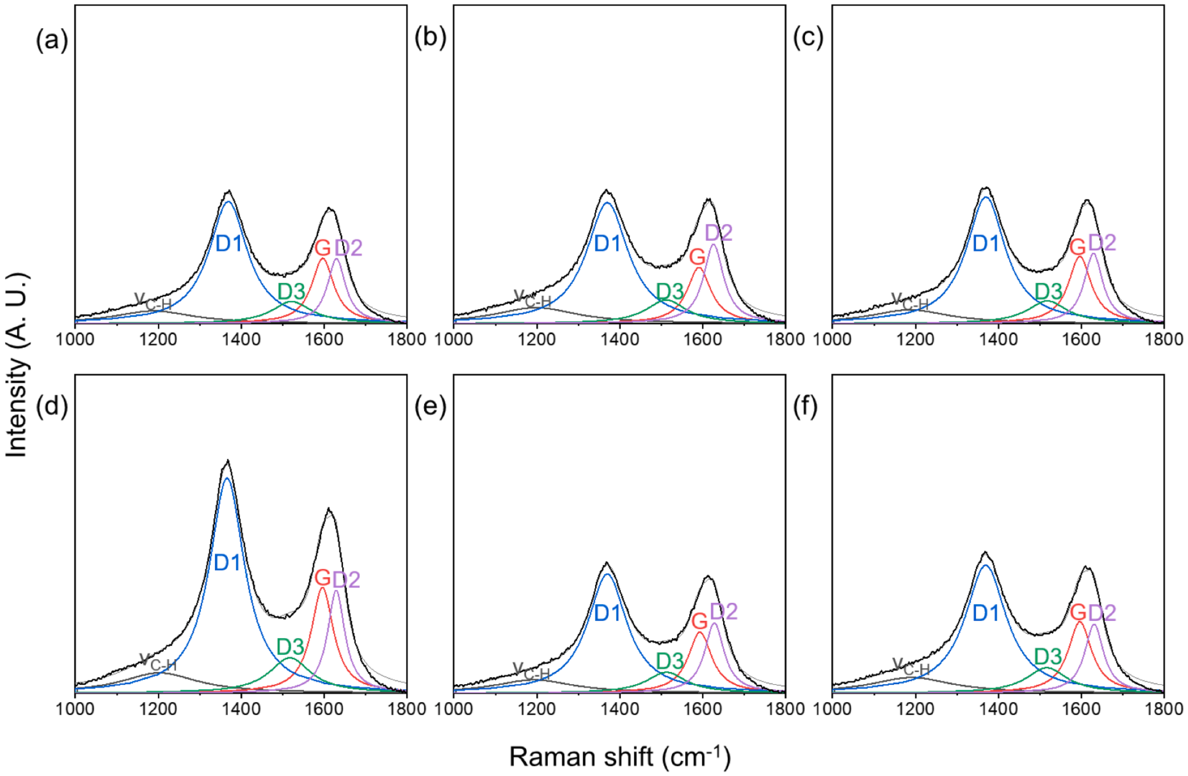

Fig. 6. Raman spectra of used (a) fused SiO_2, (b) 1.0Fe-SiO_2, and 0.5Me1.0Fe-SiO_2 catalysts (Me = (c) Co, (d) Ni, (e) Pd, (f) Pt) after a 10 h-methane conversion reaction.

Table 3
Characteristic fraction of deconvoluted area of bands assigned in the Raman spectra of fused SiO_2, 1.0Fe-SiO_2, and 0.5Me1.0Fe-SiO_2 (Me = Co, Ni, Pd, Pt) catalysts after a 10 h-methane conversion reaction.

Catalyst	I_{C-H} (%)[a]	I_{D1} (%)[a]	I_{D3} (%)[a]	I_G (%)[a]	I_{D2} (%)[a]	P_G (cm^{-1})	I_G/I_{D2}
Fused SiO_2	10.8	51.1	9.5	15.8	12.8	1597	3.23
1.0Fe-SiO_2	12.8	49.4	9.2	13.1	15.5	1591	3.78
0.5Co1.0Fe-SiO_2	10.9	50.7	9.2	15.8	13.4	1597	3.21
0.5Ni1.0Fe-SiO_2	10.4	51.6	9.9	16.0	12.1	1596	3.23
0.5Pd1.0Fe-SiO_2	11.2	49.9	8.9	15.5	14.6	1593	3.23
0.5Pt1.0Fe-SiO_2	11.9	50.1	9.8	15.9	12.3	1597	3.15

[a] Calculated from deconvoluted peak area of Raman spectra in Fig. 6.

20–50 nm entrapped in the SiO_2 structure were observed in the 1.0Fe-SiO_2 catalyst. In 0.5Co1.0Fe-SiO_2, 0.5Ni1.0Fe-SiO_2, and 0.5Pd1.0Fe-SiO_2, the second metal was located in the same position as Fe, indicating the formation of MeFe alloy particles. In 0.5Pt1.0Fe-SiO_2, Pt atoms were highly dispersed on the surface, regardless of the Fe position. As indicated by the TEM images of the as-prepared and used catalysts (Fig. S8), 0.5Pd1.0Fe-SiO_2 showed an aggregation of PdFe alloy particles, with no entrapped-metal-particle aggregation in the other catalysts. This could be attributed to the high reducibility of the weak Pd-Si metal-support interactions of the PdFe alloy in the as-prepared catalyst.

3.4. Reaction energetics

An energetic study using DFT calculations was used to theoretically understand the role of the bimetallic sites in the MTOAH. Fe_3C (001) was assumed to be the Fe-surface model structure because of its stability at high temperatures [39]. Table S5 shows the free formation energies for H*, CH_3*, CH_2*, CH*, and C*. Among all the surfaces analyzed, the Pd-Fe_3C (001) surface showed the most exergonic states for H* (-1.92 eV) and CH_3* + H* (-1.39 eV), indicating high methane activation by the Pd-Fe_3C bimetallic surface due to its strong H* binding energy. The Co-Fe_3C (001) and Ni-Fe_3C (001) surfaces showed relatively positive formation energies for H* and CH_3* + H*. Notably, the Pt-Fe_3C (001) surface exhibited a more exergonic state for CH_3*+ H* (-0.08 eV), despite its weaker H* binding energy compared to that of the Fe_3C (001) surface. Thus, the Pd-Fe_3C and Pt-Fe_3C bimetallic surfaces exhibited higher methane activation than the Fe_3C surface.

Fig. 9 shows the relative free energy diagrams for sequential reaction steps of CH_4 (g) dehydrogenation to C* + 4H* over Fe_3C (001) and Me-Fe_3C (001) (Me = Co, Ni, Pd, Pt) surfaces. Among the surfaces, Pd-Fe_3C (001) surface exhibited most exergonic states. This implies that Pd-Fe bimetallic site is vulnerable for coke deposition in spite of its high activity in methane conversion. Interestingly, Pt-Fe_3C (001) surface showed less exergonic step for the CH_2* dehydrogenation (CH_2* + 2H* → CH* + 3H*, $\triangle G$ = -0.06 eV) compared to other catalysts. Because the relative stability of CH_3* and CH_2* compared to CH* and C* implies the low coke selectivity in methane direct conversion, Pt-Fe_3C bimetallic site is expected to be favorable for methane activation while suppressing coke formation [46].

To investigate the stability of the C_2 intermediates on the bimetallic

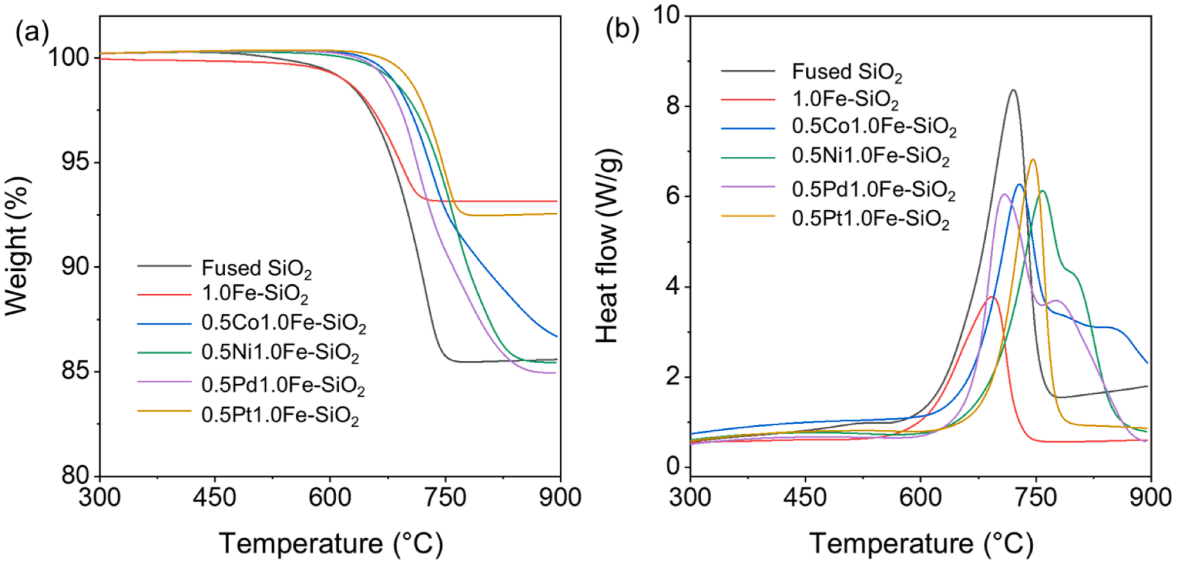

Fig. 7. (a) TG and (b) DTA profiles of used catalysts after a 10 h-reaction.

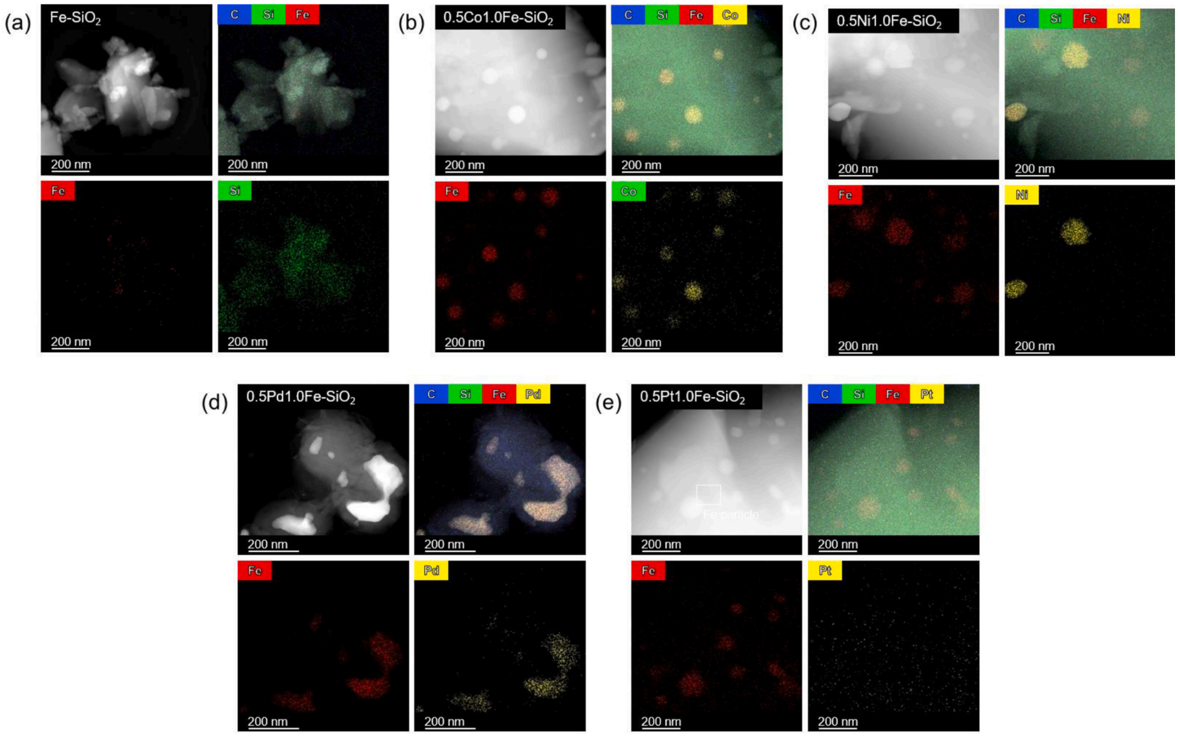

Fig. 8. HAADF and TEM-EDS mapping images of used (a) 1.0Fe-SiO$_2$, 0.5Me1.0Fe-SiO$_2$ (Me = (b) Co, (c) Ni, (d) Pd, (e) Pt) catalysts after a 10 h-methane conversion reaction.

surfaces, the energetics for $C_2H_5^*$ dehydrogenation were analyzed (Fig. 10). The significantly low selectivity of C_2H_6 in MTOAH and the C_2-hydrogenation results (Figs. 2–4, and Table 2) indicated that C_2H_6 easily generated $C_2H_5^*$ radicals in the gas phase at high temperatures [7]. Therefore, the energetics of $C_2H_5^*$ dehydrogenation and competitive $C_2H_4^*$ desorption were used to estimate the activity of the bimetallic sites. The activation energies for the initial $C_2H_5^*$-dehydrogenation step exhibited by the Ni-Fe$_3$C (001) (1.19 eV), Co-Fe$_3$C (001) (0.88 eV), and Pd-Fe$_3$C (001) (1.06 eV) surfaces were significantly lower than that over Fe$_3$C (001) (1.42 eV), which was similar to that exhibited by the Pt-Fe$_3$C surface (1.39 eV). On the Pd-Fe$_3$C (001) surface, the subsequent dehydrogenation of $C_2H_4^*$ required an exergonic state with a relatively low activation energy, while the C_2H_4 desorption step required an endergonic state ($C_2H_4^* + H^* \rightarrow C_2H_4\ (g) + H^*$, $\Delta G = 0.17$ eV). Thus, the Pd-Fe sites promoted the production of acetylene, the major coke precursor, by the dehydrogenation of the C_2 intermediates, consistent with the high coke selectivity of the 0.5Pd1.0Fe-SiO$_2$ catalyst for MTOAH (Table 2). In $C_2H_4^*$ dehydrogenation, the Pt-Fe$_3$C surface showed the higher activation energies for $C_2H_3^*$ dehydrogenation ($\Delta G = 1.75$ eV) and $C_2H_2^*$ dehydrogenation ($\Delta G = 1.09$ eV) compared to Fe$_3$C surface ($\Delta G = 1.16$ eV and 0.95 eV). This implies that Pt-Fe$_3$C surface inhibits graphitic coke formation by C_2 dehydrogenation compared to Fe$_3$C surface. This result is also in agreement with the lowest I_G/I_{D2} ratio of the used 0.5Pt1.0Fe-SiO$_2$ catalyst in the Raman spectroscopy result (Table 3).

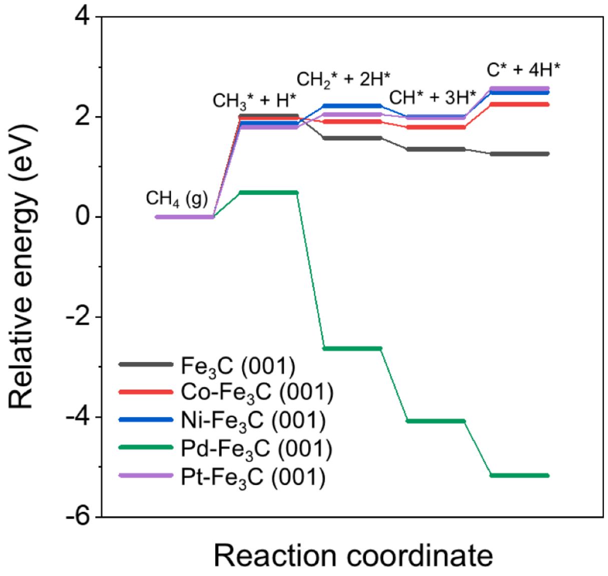

Fig. 9. Relative energy diagrams for CH_4 (g) dehydrogenation over Fe_3C (001), Co-Fe_3C (001), Ni-Fe_3C (001), Pd-Fe_3C (001), and Pt-Fe_3C (001) at 1020°C, 1 bar.

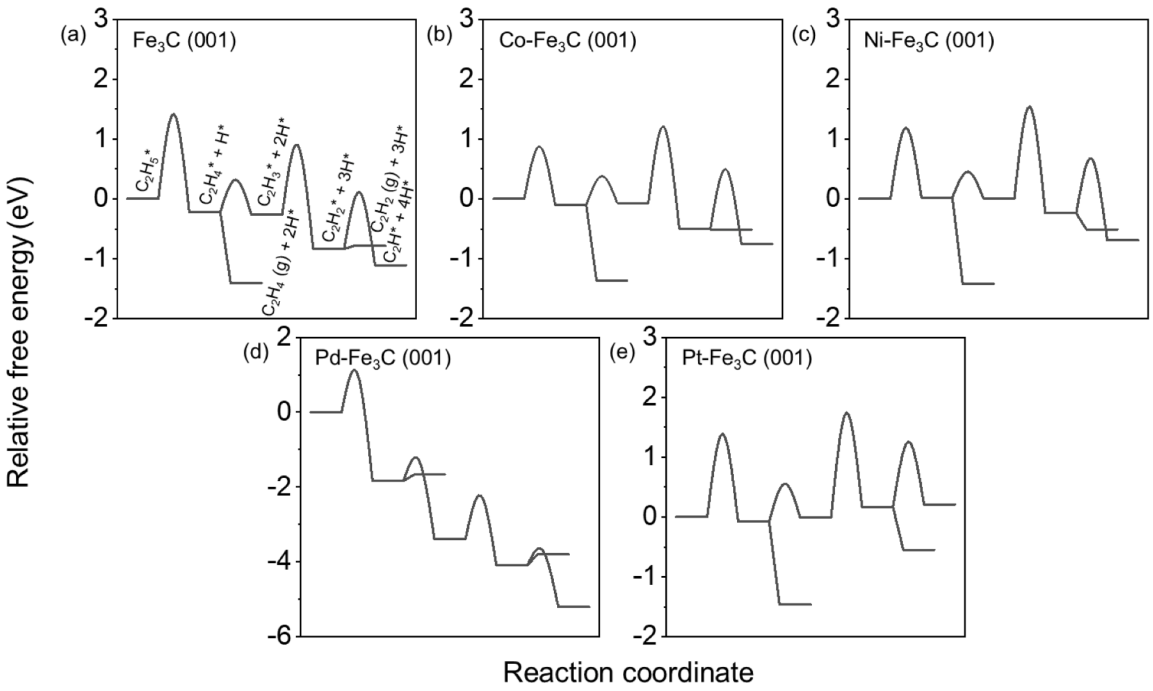

Fig. 10. Relative energy diagrams for C_2H_5* dehydrogenation over (a) Fe_3C (001), (b) Co-Fe_3C (001), (c) Ni-Fe_3C (001), (d) Pd-Fe_3C (001), and (e) Pt-Fe_3C (001) at 1020°C, 1 bar.

4. Conclusion

Here, MeFe-SiO_2 (Me = Co, Ni, Pd, Pt) catalysts with bimetallic sites entrapped in a highly crystalline SiO_2 structure were synthesized and used for direct methane conversion to olefins, aromatics, and hydrogen at 1020°C. Among the synthesized catalysts, 0.5Pt1.0Fe-SiO_2 exhibited the highest aromatic selectivity (37.1%) with a high methane conversion (10.0%). The influence of the bimetallic sites on MTOAH, with respect to methane activation and C_2 dehydrogenation was experimentally and theoretically analyzed. Under MTOAH conditions, coke deposition occurs in the order of $C_2H_6 < C_2H_4 < C_2H_2$, indicating that acetylene is the major coke precursor. Computational analysis showed that the Pt-Fe bimetallic sites favored methane activation and inhibited graphitic coke formation by C_2 dehydrogenation. This study highlights the importance of controlling stability of reaction intermediates and the potential applicability of Pt-Fe bimetallic catalysts with enhanced hydrocarbon selectivity in MTOAH.

CRediT authorship contribution statement

Seung Ju Han: Formal analysis, Writing – original draft, Data curation, Writing – review & editing. **Tsegay Gebrekidan Gebreyohannes:** Data curation, Methodology, Writing – review & editing. **Sung Woo lee:** Data curation, Methodology. **Seok Ki Kim:** Data curation, Methodology. **Hyun Woo Kim:** Formal analysis, Data curation. **Jungho Shin:** Formal analysis, Data curation. **Yong Tae Kim:** Funding acquisition, Project administration.

Declaration of Competing Interest

The authors declare that they have no known competing financial interests or personal relationships that could have appeared to influence the work reported in this paper.

Data availability

Data will be made available on request.

Acknowledgements

This research was supported by the C1 Gas Refinery Program through the National Research Foundation of Korea (NRF) funded by the Ministry of Science, ICT & Future Planning (NRF-2017M3D3A1A01037001). This study was financially supported by the KRICT Project (SI2211-30) of the Korea Research Institute of Chemical Technology.

Supplementary materials

Supplementary material associated with this article can be found, in the online version, at doi:10.1016/j.mcat.2022.112864.

References

[1] Y.M. Alshammari, Scenario analysis for energy transition in the chemical industry: An industrial case study in Saudi Arabia, Energy Policy 150 (2021), 112128.

[2] P. Schwach, X. Pan, X. Bao, Direct Conversion of Methane to Value-Added Chemicals over Heterogeneous Catalysts: Challenges and Prospects, Chem. Rev. 117 (2017) 8497–8520.

[3] E.V. Kondratenko, T. Peppel, D. Seeburg, V.A. Kondratenko, N. Kalevaru, A. Martin, S. Wohlrab, Methane conversion into different hydrocarbons or oxygenates: current status and future perspectives in catalyst development and reactor operation, Catal. Sci. Technol. 7 (2017) 366–381.

[4] L. Wang, L. Tao, M. Xie, G. Xu, J. Huang, Y. Xu, Dehydrogenation and aromatization of methane under non-oxidizing conditions, Catal. Lett. 21 (1993) 35–41.

[5] Z.R. Ismagilov, E.V. Matus, L.T. Tsikoza, Direct conversion of methane on Mo/ZSM-5 catalysts to produce benzene and hydrogen: achievements and perspectives, Energy Environ. Sci. 1 (2008) 526.

[6] N. Kosinov, E.A. Uslamin, L. Meng, A. Parastaev, Y. Liu, E.J.M. Hensen, Reversible Nature of Coke Formation on Mo/ZSM-5 Methane Dehydroaromatization Catalysts, Angew. Chem.-Int. Edit. 58 (2019) 7068–7072.

[7] A. Holmen, O. Olsvik, O.A. Rokstad, Pyrolysis of natural gas: chemistry and process concepts, Fuel Process. Technol. 42 (1995) 249–267.

[8] X. Guo, G. Fang, G. Li, H. Ma, H. Fan, L. Yu, C. Ma, X. Wu, D. Deng, M. Wei, D. Tan, R. Si, S. Zhang, J. Li, L. Sun, Z. Tang, X. Pan, X. Bao, Direct, nonoxidative conversion of methane to ethylene, aromatics, and hydrogen, Science 344 (2014) 616–619.

[9] S.K. Kim, H.W. Kim, S.J. Han, S.W. Lee, J. Shin, Y.T. Kim, Mechanistic and microkinetic study of non-oxidative methane coupling on a single-atom iron catalyst, Comm. Chem. 3 (2020) 58.

[10] P. Xie, T. Pu, A. Nie, S. Hwang, S.C. Purdy, W. Yu, D. Su, J.T. Miller, C. Wang, Nanoceria-Supported Single-Atom Platinum Catalysts for Direct Methane Conversion, ACS Catal 8 (2018) 4044–4048.

[11] Y. Liu, J.C. Liu, T.H. Li, Z.H. Duan, T.Y. Zhang, M. Yan, W.L. Li, H. Xiao, Y. G. Wang, C.R. Chang, J. Li, Unravelling the Enigma of Nonoxidative Conversion of Methane on Iron Single-Atom Catalysts, Angew. Chem.-Int. Edit. 59 (2020) 18586–18590.

[12] S.J. Han, S.W. Lee, H.W. Kim, S.K. Kim, Y.T. Kim, Nonoxidative Direct Conversion of Methane on Silica-Based Iron Catalysts: Effect of Catalytic Surface, ACS Catal 9 (2019) 7984–7997.

[13] G.K. Dixit, M. Kumar, A. Katiyar, A.P.J. Jansen, A.P. van Bavel, R. Agrawal, P. M. Shenai, V. Srinivasan, Unraveling the activity of iron carbide clusters embedded in silica for thermocatalytic conversion of methane, Catal. Sci. Technol. 11 (2021) 7398–7411.

[14] R.S. Postma, L. Lefferts, Influence of Axial Temperature Profiles on Fe/SiO_2 Catalyzed Non-oxidative Coupling of Methane, ChemCatChem 13 (2021) 1157–1160.

[15] H.E. Toraman, K. Alexopoulos, S.C. Oh, S. Cheng, D. Liu, D.G. Vlachos, Ethylene production by direct conversion of methane over isolated single active centers, Chem. Eng. J. 420 (2021), 130493.

[16] S.C. Oh, E. Schulman, J. Zhang, J. Fan, Y. Pan, J. Meng, D. Liu, Direct Non-Oxidative Methane Conversion in a Millisecond Catalytic Wall Reactor, Angew. Chem.-Int. Edit. 131 (2019) 7157–7160.

[17] J. Hao, P. Schwach, G. Fang, X. Guo, H. Zhang, H. Shen, X. Huang, D. Eggart, X. Pan, X. Bao, Enhanced Methane Conversion to Olefins and Aromatics by H-Donor Molecules under Nonoxidative Condition, ACS Catal 9 (2019) 9045–9050.

[18] J. Hao, P. Schwach, L. Li, X. Guo, J. Weng, H. Zhang, H. Shen, G. Fang, X. Huang, X. Pan, C. Xiao, X. Yang, X. Bao, Direct experimental detection of hydrogen radicals in non-oxidative methane catalytic reaction, J. Energy Chem. 52 (2021) 372–376.

[19] K. Huang, J.B. Miller, G.W. Huber, J.A. Dumesic, C.T. Maravelias, A General Framework for the Evaluation of Direct Nonoxidative Methane Conversion Strategies, Joule 2 (2018) 349–365.

[20] M.A. Abedin, S. Kanitkar, S. Bhattar, J.J. Spivey, Promotional Effect of Cr in Sulfated Zirconia-Based Mo Catalyst for Methane Dehydroaromatization, Energy Technol 8 (2019), 1900555.

[21] N. Kosinov, F.J.A.G. Coumans, E.A. Uslamin, A.S.G. Wijpkema, B. Mezari, E.J. M. Hensen, Methane Dehydroaromatization by Mo/HZSM-5: Mono- or Bifunctional Catalysis? ACS Catal 7 (2016) 520–529.

[22] A. Sridhar, M. Rahman, S.J. Khatib, Enhancement of Molybdenum/ZSM-5 Catalysts in Methane Aromatization by the Addition of Iron Promoters and by Reduction/Carburization Pretreatment, ChemCatChem 10 (2018) 2571–2583.

[23] S. Kanitkar, M.A. Abedin, S. Bhattar, J.J. Spivey, Methane dehydroaromatization over molybdenum supported on sulfated zirconia catalysts, Appl. Catal. A-Gen. 575 (2019) 25–37.

[24] A. Sridhar, M. Rahman, A. Infantes-Molina, B.J. Wylie, C.G. Borcik, S.J. Khatib, Bimetallic Mo-Co/ZSM-5 and Mo-Ni/ZSM-5 catalysts for methane dehydroaromatization: A study of the effect of pretreatment and metal loadings on the catalytic behavior, Appl. Catal. A-Gen. 589 (2020), 117247.

[25] T. Zhang, Recent advances in heterogeneous catalysis for the nonoxidative conversion of methane, Chem. Sci. 12 (2021) 12529–12545.

[26] X. Cheng, P. Yan, X. Zhang, F. Yang, C. Dai, D. Li, X.-X. Ma, Enhanced methane dehydroaromatization in the presence of CO_2 over Fe- and Mg-modified Mo/ZSM-5, Mol. Catal. 437 (2017) 114–120.

[27] Y. Xiao, A. Varma, Highly Selective Nonoxidative Coupling of Methane over Pt-Bi Bimetallic Catalysts, ACS Catal 8 (2018) 2735–2740.

[28] P. Ni, L. Cao, T. Zhu, G. Zhao, Y. Liu, Y. Lu, Nonoxidative coupling of methane to olefins and aromatics over molten W-In bimetal catalyst, Fuel 316 (2022), 123333.

[29] Q. Chang, C. Zhang, C. Liu, K. Li, Y. Yun, A.V. Cheruvathur, Y. Yang, Y. Li, Facile Large-Scale Synthesis of Nanoscale Fayalite, α-Fe_2SiO_4, ChemistrySelect 2 (2017) 3356–3361.

[30] M.J. Boruah, A. Gogoi, B.C. Nath, G.A. Ahmed, Light scattering studies of randomly oriented polycrystalline fayalite micro particles as interstellar dust analogues, J. Quant. Spectrosc. Radiat. Transf. 196 (2017) 213–221.

[31] S. Lowell, J.E. Shields, M.A. Thomas, M. Thommes, Characterization of porous solids and powders: Surface area, pore size and density, Springer, 2012.

[32] G. Kresse, J. Hafner, Ab initio molecular-dynamics simulation of the liquid-metal-amorphous-semiconductor transition in germanium, Phys. Rev. B-Condens Matter 49 (1994) 14251–14269.

[33] G. Kresse, J. Furthmüller, Efficiency of ab-initio total energy calculations for metals and semiconductors using a plane-wave basis set, Comput. Mater. Sci. 6 (1996) 15–50.

[34] M. Dion, H. Rydberg, E. Schroder, D.C. Langreth, B.I. Lundqvist, van der Waals density functional for general geometries, Phys. Rev. Lett. 92 (2004), 246401.

[35] J. Klimeš, D.R. Bowler, A. Michaelides, Van der Waals density functionals applied to solids, Phys. Rev. B 83 (2011), 195131.

[36] G. Roman-Perez, J.M. Soler, Efficient implementation of a van der Waals density functional: application to double-wall carbon nanotubes, Phys. Rev. Lett. 103 (2009), 096102.

[37] K. Lee, É.D. Murray, L. Kong, B.I. Lundqvist, D.C. Langreth, Higher-accuracy van der Waals density functional, Phys. Rev. B 82 (2010), 081101.

[38] X. Ma, A. Genest, L. Spanu, N. Rösch, Structures and vibrational frequencies of CO adsorbed on transition metals from calculations using the vdW-DF2 functional, Comput. Theor. Chem. 1069 (2015) 147–154.

[39] W. Chiou, Structure and stability of Fe_3C-cementite surfaces from first principles, Surf. Sci. 530 (2003) 88–100.

[40] S.J. Han, S.-M. Hwang, H.-G. Park, C. Zhang, K.-W. Jun, S.K. Kim, Identification of active sites for CO_2 hydrogenation in Fe catalysts by first-principles microkinetic modelling, J. Mater. Chem. A 8 (2020) 13014–13023.

[41] C.J. Cramer, Essentials of Computational Chemistry, Wiley, 2004. Second Edition ed.

[42] G.D. Nipan, Phase states of Li/W/Mn/SiO_2 composites in catalytic oxidative coupling of methane, Inorganic Materials 51 (2015) 389–395.

[43] C. Guéret, M. Daroux, F. Billaud, Methane pyrolysis: thermodynamics, Chem. Eng. Sci. 52 (1997) 815–827.

[44] P. Castaño, G. Elordi, M. Olazar, A.T. Aguayo, B. Pawelec, J. Bilbao, Insights into the coke deposited on HZSM-5, Hβ and HY zeolites during the cracking of polyethylene, Appl. Catal. B-Environ. 104 (2011) 91–100.

[45] C. Li, P.C. Stair, Ultraviolet Raman spectroscopy characterization of coke formation in zeolites, Catalysis Today 33 (1997) 353–360.

[46] M. Yoshida, Y. Tsuji, S. Iguchi, H. Nishiguchi, I. Yamanaka, H. Abe, T. Kamachi, K. Yoshizawa, Toward Computational Screening of Bimetallic Alloys for Methane Activation: A Case Study of MgPt Alloy, ACS Catal 12 (2022) 9458–9472.